Zirconium-based Metal-Organic Frameworks as Reusable Antibacterial Peroxide Carriers for Protective Textiles

Kaikai Ma,[*,†,#] Yuk Ha Cheung,[*,‡,#] Haomiao Xie,[†,#] Xingjie Wang,[†] Michael Evangelopoulos,[†,&] Kent O. Kirlikovali,[†] Shengyi Su,[†] Xiaoliang Wang,[†] Chad A. Mirkin,[†] John Xin,[*,‡] and Omar K. Farha[*,†,⊥]

[†]International Institute for Nanotechnology, Institute for Sustainability and Energy at Northwestern, and Department of Chemistry, Northwestern University, 2145 Sheridan Road, Evanston, Illinois 60208, United States

[‡]Research Centre for Smart Wearable Technology, School of Fashion and Textiles, The Hong Kong Polytechnic University, Kowloon 999077, Hong Kong SAR

[&]Department of Chemical and Biological Engineering, Northwestern University, 2145 Sheridan Road, Evanston, Illinois 60208, United States

[⊥]Department of Chemical and Biological Engineering, Northwestern University, 2145 Sheridan Road, Evanston, Illinois 60208, United States

ABSTRACT

Countries around the world have sought efficient protective coverings, including masks, gowns, and fabrics, for air purification to protect people against infectious diseases. However, the demand for significant quantities of disposable protective textiles poses a global challenge, especially when the production of protective gear is suspended due to COVID–19 outbreaks in factories and along supply lines. Therefore, the development of reusable, self-decontaminating protective masks and coverings loaded with disinfectants, such as antibacterial peroxide species, presents an attractive strategy to fight against bacteria risks. In this work, we incorporated persulfate ions, which serve as stable active peroxide precursors, into two porous zirconium-based metal–organic frameworks (Zr-MOFs), enabling these materials to act as regenerable reservoirs for the slow release of biocidal hydrogen peroxide upon hydrolysis by contact with humid air. Single-crystal X-ray diffraction studies reveal the two different coordination motifs for the persulfate ions, which can either bridge between two adjacent nodes or coordinate to a single node depending on both the node connectivity and the distances between open metal sites. The active peroxide precursors within the porous Zr-MOF carriers are stable during storage and easily regenerated once consumed. Importantly, these persulfate-loaded Zr-MOFs can be integrated onto textiles using a facile aqueous *in-situ* growth procedure, and these composites demonstrate potent and reusable biocidal activity against both Gram-negative bacteria and Gram-positive bacteria. Overall, this approach presents a viable strategy to develop robust protective textiles capable of rapidly deactivating pathogens.

Introduction

The global community is under threat from high-risk pathogenic bacteria.[1-4] Personal protective garments and textile air purification filters are imperative to combat these biological threats and protect both vulnerable healthcare personnel and the general public. However, most protective textiles and masks currently in use only act as physical barriers of the pathogens to protect the user from exposure. Unfortunately, pathogens are detectable on these contaminated textiles for several days following exposure, increasing the risks of cross-infection of disease.[5-8] One promising strategy to decrease infections from bacterial pathogens involves functionalizing the textile with a reusable and active protective layer that deactivates pathogens upon exposure.[9-18] In particular, loading disinfecting species, such as active halogens (e.g., chloramine or I_2) and active peroxide species (e.g., peroxide), into a textile coated with a porous carrier layer may present access to self-cleaning biocidal protective textiles that could slowly release the active species and be repeatedly loaded for many cycles with no loss in performance.[19-25]

Metal−organic frameworks (MOFs) are a class of nanoporous crystalline porous materials comprised of metal ion- or cluster-based nodes and organic linkers, and the large chemical diversity of available building blocks enables excellent control over physical properties that has established MOFs as high-performance materials in a variety of fields.[26-31] For example, their highly porous nature makes MOFs ideal candidates for host-guest applications for the loading and release of biologically active species.[32-39] Previously, researchers have developed MOF-based carriers by loading active species (e.g., chloramine or I_2) into MOF nanopores and observed good biocidal performance from these MOF-coated fiber composites towards pathogens.[38-39] However, the short shelf-lives caused by weak MOF-halogen bonding interactions, as well as the unwanted odor and color of halogen-based biocidal materials, has created difficulties in popularizing MOF-coated protective textiles and hindered their use in practical biocidal applications.

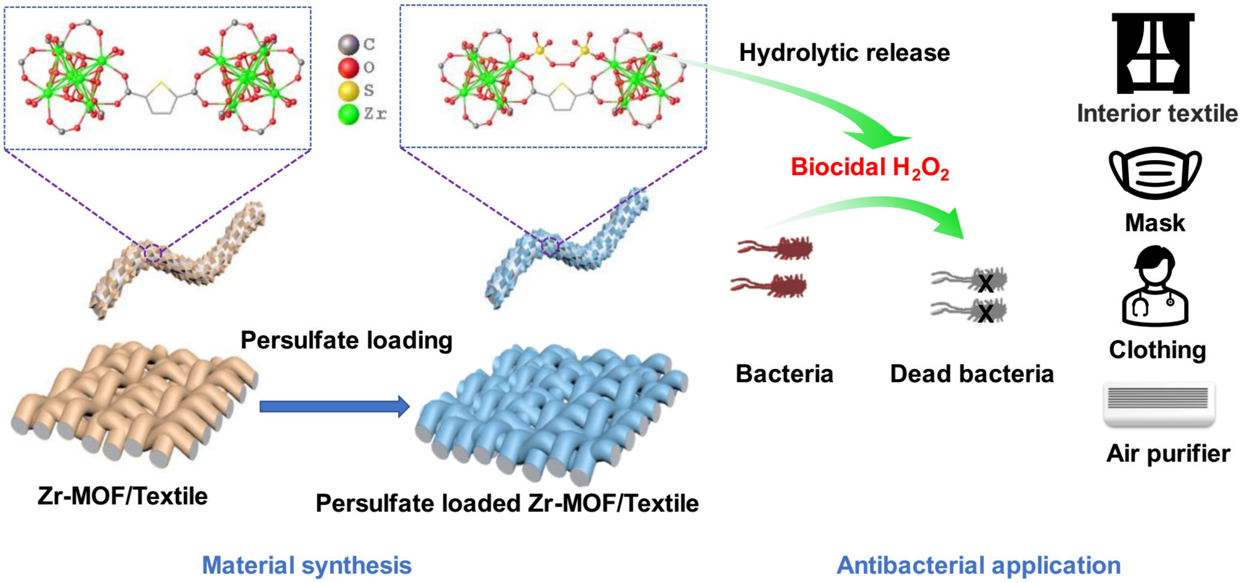

Scheme 1. The schematic representation of the persulfate loaded Zr-MOF/textile composite for antibacterial application.

To address these limitations, we developed a new strategy in which we loaded zirconium-based MOFs (Zr-MOFs) with stable and regenerable hydrogen peroxide precursors, namely persulfate (PSO), which slowly releases user-friendly biocidal hydrogen peroxide upon hydrolysis by contact with humid air (Scheme 1). Specifically, we post-synthetically incorporated PSO into the Zr_6 nodes of two nanoporous zirconium-based MOFs (Zr-MOFs), MOF-808 (with 6-connected Zr_6 nodes) and DUT-67 (with 8-connected Zr_6 nodes), by taking advantage of the accessible open metal sites on the Zr_6 nodes. Single crystal X-ray diffraction (SCXRD) crystallographic studies verified the coordination modes of the PSO ions to the Zr_6 nodes. Unlike the reported MOF-based carriers in the literature that rely on the physical adsorption of the active species inside the cavities, the formation of coordinating bonds between Zr_6 nodes and PSO ions prevents the leaching of the active component precursor to the environment. On the other hand, the coordination bonds formed are reversible enough in aqueous solution at room temperature to enable repeatable PSO loadings for several cycles by simply exchanging the inactive, discharged species with a fresh PSO solution in mild conditions. Moreover, we employed an aqueous *in-situ* growth method to coat these two Zr-MOFs onto a textile fiber, and PSO loading into the composites afforded durable and regenerable biocidal protective fabrics (Scheme 1). Cytotoxicity studies showcased favorable biocompatibility of the MOF/textile composites to mammalian cells, which further demonstrates the potential practical values of these new composites as antibacterial textile materials.

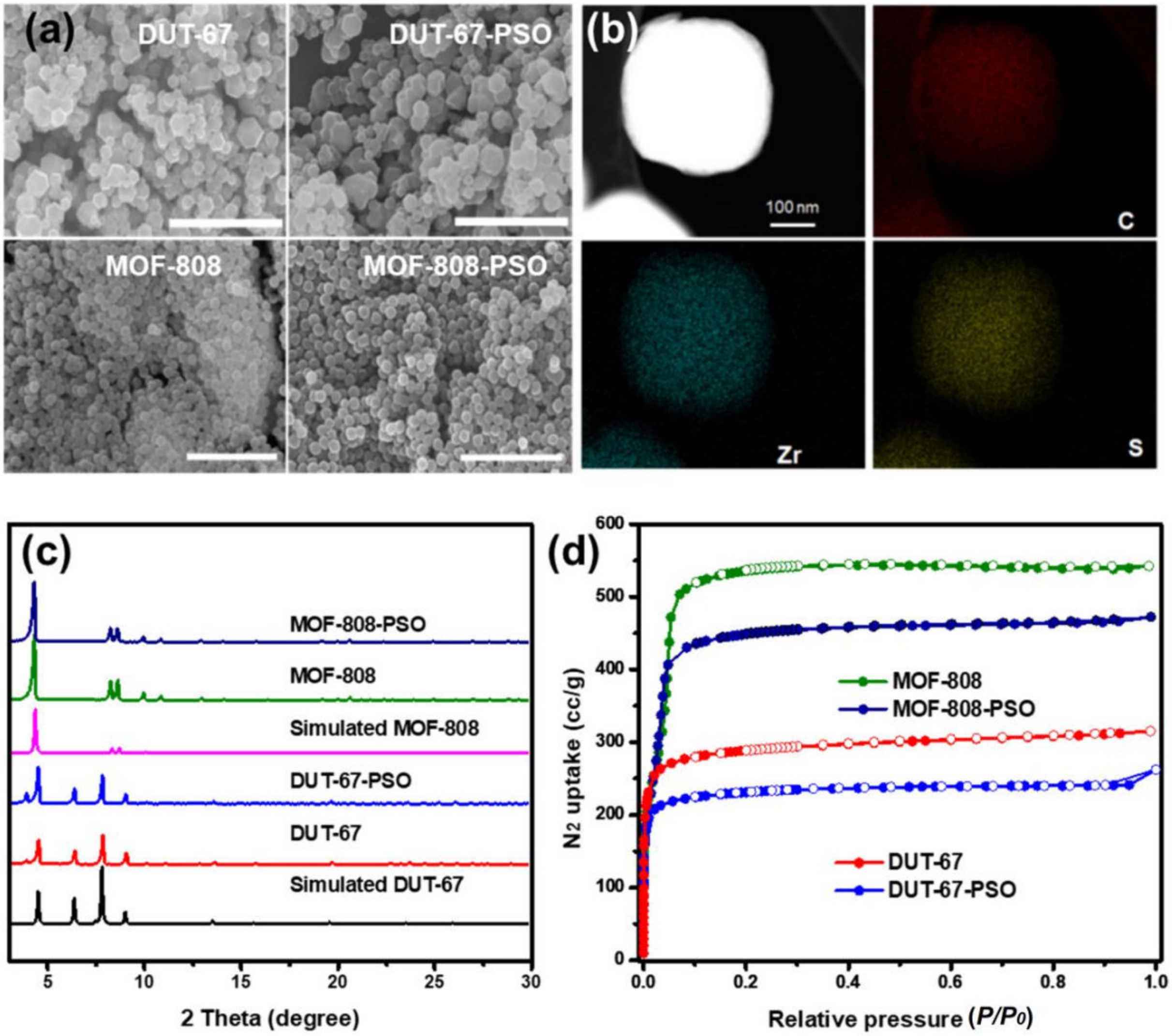

Figure 1. (a) SEM images of DUT-67 and MOF-808 before and after PSO loading. Scale bars: 5 μm. (b) EDX mapping of MOF-808-PSO. (c) PXRD and (d) N_2 sorption isotherms of the samples.

Results and Discussion

Structure Studies of Persulfate-loaded Zr-MOFs

To begin our investigation, we selected two nanoporous zirconium-based MOFs (Zr-MOFs), DUT-67 and MOF-808, due to their structural robustness and accessible Zr_6 nodes that are amenable to the post-synthetic immobilization of functional anions.[40-42] To load the active peroxide precursor, PSO, into the frameworks, we incubated powdered DUT-67 or MOF-808 in a 5 wt% sodium persulfate solution at room temperature for 24 h. Scanning electron microscopy (SEM) images reveal that the resulting PSO-loaded MOFs, denoted as DUT-67-PSO and MOF-808-PSO, exhibit the same morphology as those of the original materials (Figure 1a). Next, we verified the successful incorporation of PSO peroxide precursors into the Zr-MOFs through a series of experiments. First, energy dispersive X-ray (EDX) mapping studies confirmed the uniform distribution of sulfur throughout MOF-808-PSO particles (Figure 1b). Then, a potassium iodine oxidation test qualitatively confirmed the presence of oxidizing species in the PSO-loaded MOF materials (Figure S1).[23] For example, mixing MOF-808-PSO or DUT-67-PSO with a potassium iodide solution afforded an immediate color change from white to deep brown, which indicated the formation of iodine upon reaction with the oxidizing PSO; in contrast, addition of the same potassium iodide solution to the parent MOFs did not induce any color change (Figure S1). We then quantified the active peroxide loading, namely the weight percentage of the active peroxide, in the PSO-loaded MOFs through an iodometric/thiosulfate titration. The active peroxide loadings in MOF-808-PSO and DUT-67-PSO are 3.0 wt% and 2.7 wt%, respectively. The loading values correspond to about 1.7 and 1.4 PSO loaded onto each Zr_6 node, respectively, and are similar to the PSO loadings of 1.9 and 1.5 per Zr_6 node, respectively, determined from sulfur content analysis of inductively coupled plasma-optical emission spectroscopy (ICP-OES) experiments. X-ray photoelectron spectroscopy (XPS) experiments also verified the introduction of PSO by revealing the presence of the characteristic sulfur element from PSO in the MOFs (Figure S2-S4). The PSO loading based on XPS analysis is 1.7 and 1.3 per Zr_6 node on MOF-808-PSO and DUT-67-PSO respectively, further corroborating the successful immobilization of PSO onto Zr-MOFs. Importantly, these PSO loadings were achieved through treatment of Zr-MOFs with aqueous solutions at room temperature without any pH adjustment, highlighting the practicality of this strategy to incorporate active peroxide precursors into the frameworks. The powder X-ray diffraction (PXRD) patterns of the PSO-loaded MOFs are comparable to those of the pristine MOFs, confirming the retention of the crystalline structure following PSO incorporation (Figure 1c).[40-42] Finally, we probed the nanoporosity of these MOFs using N_2 sorption isotherms at 77 K and observed a slightly reduced adsorption capacity for both MOFs following PSO loading (Figure 1d), e.g. 540 cc/g (25 mmol/g) to 460 cc/g (21 mmol/g) for MOF-808 and 310 cc/g (14 mmol/g) to 230 cc/g (10 mmol/g) for DUT-67. The pore volume of MOF-

808 was reduced from 0.9 cc/g to 0.7 cc/g and pore volume of DUT-67 was reduced from 0.4 cc/g to 0.3 cc/g, after PSO loading. The reduced N_2 sorption capacity and pore volume are due to the added weight of PSO ions within frameworks, which further proves the successful introduction of PSO into the MOF pores.

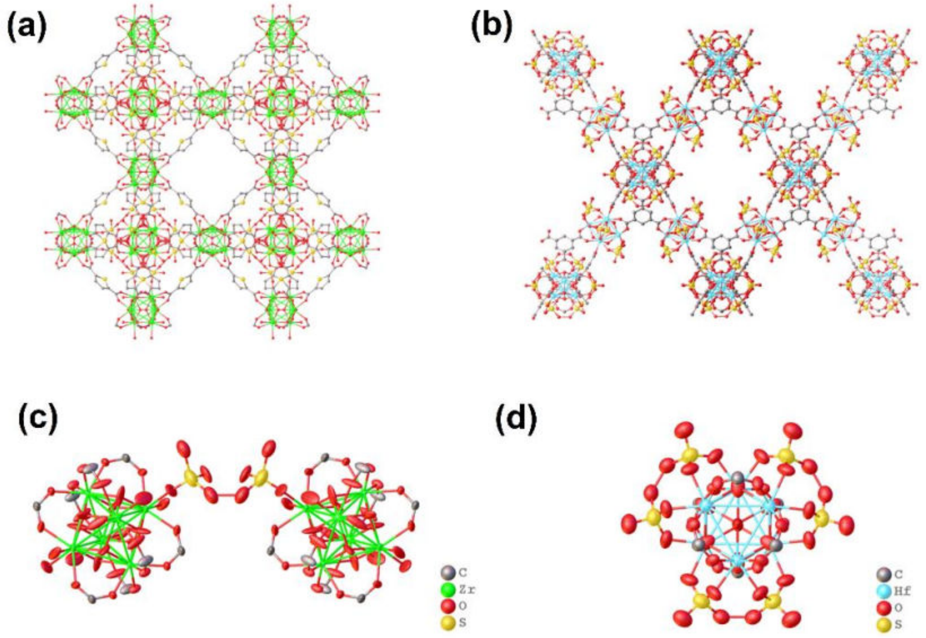

Figure 2. Crystal structures of the persulfate (PSO)-modified MOFs (a) DUT-67-PSO and (b) MOF-808(Hf)-PSO obtained from single-crystal X-ray diffraction studies. Close-up view of the coordination modes of the PSO anions on the M_6 node(s) for (c) DUT-67-PSO(Zr) (M = Zr) and (d) MOF-808(Hf)-PSO (M = Hf). Organic linkers and disordered parts are omitted for clarity.

To fully understand the atomic structure of the PSO-loaded Zr-MOFs, we first collected single crystal X-ray diffraction (SCXRD) data of DUT-67-PSO(Zr) crystals.[43] The results show that the framework structure remains unchanged (Table S1), which corroborates the PXRD results (*vide supra*). The octahedral pores feature PSO ions that can be resolved with a positional disorder related to the 3-fold symmetry of the framework (Figure 2a and Figure S5a). In the crystal structure, one PSO ion bridges two adjacent Zr_6 clusters in a monodentate fashion, with one O atom from PSO replacing one –OH group on the open metal sites that point towards the octahedral pore for each Zr_6 node (Figure 2c). The O–O bond length in PSO is 1.80(14) Å, which is relatively long compared to reported values (1.4-1.6 Å) for comparable systems,[44-47] but is still significantly shorter than the sum of Van der Waals radii of two oxygen atoms (3.0 Å). Interestingly, we did not find any evidence of PSO ions on the open metal sites pointing towards the larger, truncated cube-shaped pores, which results in a theoretical maximum loading rate of 1.33 of persulfate ions for each 8-connected Zr_6 node in DUT-67-PSO.

In contrast to DUT-67-PSO(Zr), our attempts to synthesize large MOF-808-PSO(Zr) single crystals did not provide any with suitable diffraction intensity for analysis. Therefore, we loaded PSO into MOF-808(Hf), which is isoreticular to MOF-808(Zr) and features the same M_6-based node, to improve the diffraction intensity of the crystals.[42] Analysis of the diffraction study revealed that rather than the monodentate coordination of one PSO to two adjacent nodes as in DUT-67-PSO(Zr), a single persulfate ion coordinates to two open metal sites in a bidentate fashion on one Hf_6 node in MOF-808-PSO(Hf) (Figure 2b and d). Based on this coordination geometry, the theoretical maximum incorporation rate is 3 PSO for every Hf_6 node in MOF-808-PSO(Hf) (Figure S5c-d). The O–O bond length for PSO in MOF-808-PSO(Hf) is 1.76(12) Å, which is comparable to the bond length observed in DUT-67-PSO(Zr) and suggests a similar weakening of this bond upon PSO coordination to the node.

To further elucidate the origin of the differences in PSO coordination for these two MOFs, we analyzed distances for key oxygen atoms coordinated to the M_6 nodes (M = Zr, Hf). In DUT-67-PSO(Zr), the distance between the two terminal oxygen atoms of aqua/hydroxo ligands capping the open metal sites of adjacent Zr_6 nodes that are facing towards the truncated cube pore of is 7.26 Å (Figure S6a). In comparison, the distance between the two analogous PSO-based oxygen atoms that are on the same nodes but facing towards the octahedral pore is 6.42 Å, suggesting distances beyond this might be unfavorable for PSO to bridge across two coordination sites. In contrast, the distance between the terminal PSO-based oxygen atoms that are capping the open metal of the Hf_6 node in a bidentate fashion in MOF-808(Hf)-PSO is 5.31 Å (Figure S6b). Combined, these results illustrate that the successful incorporation of persulfate ions into MOFs with this hexanuclear M_6 cluster (M = Zr, Hf) relies on suitable distances between open metal sites.

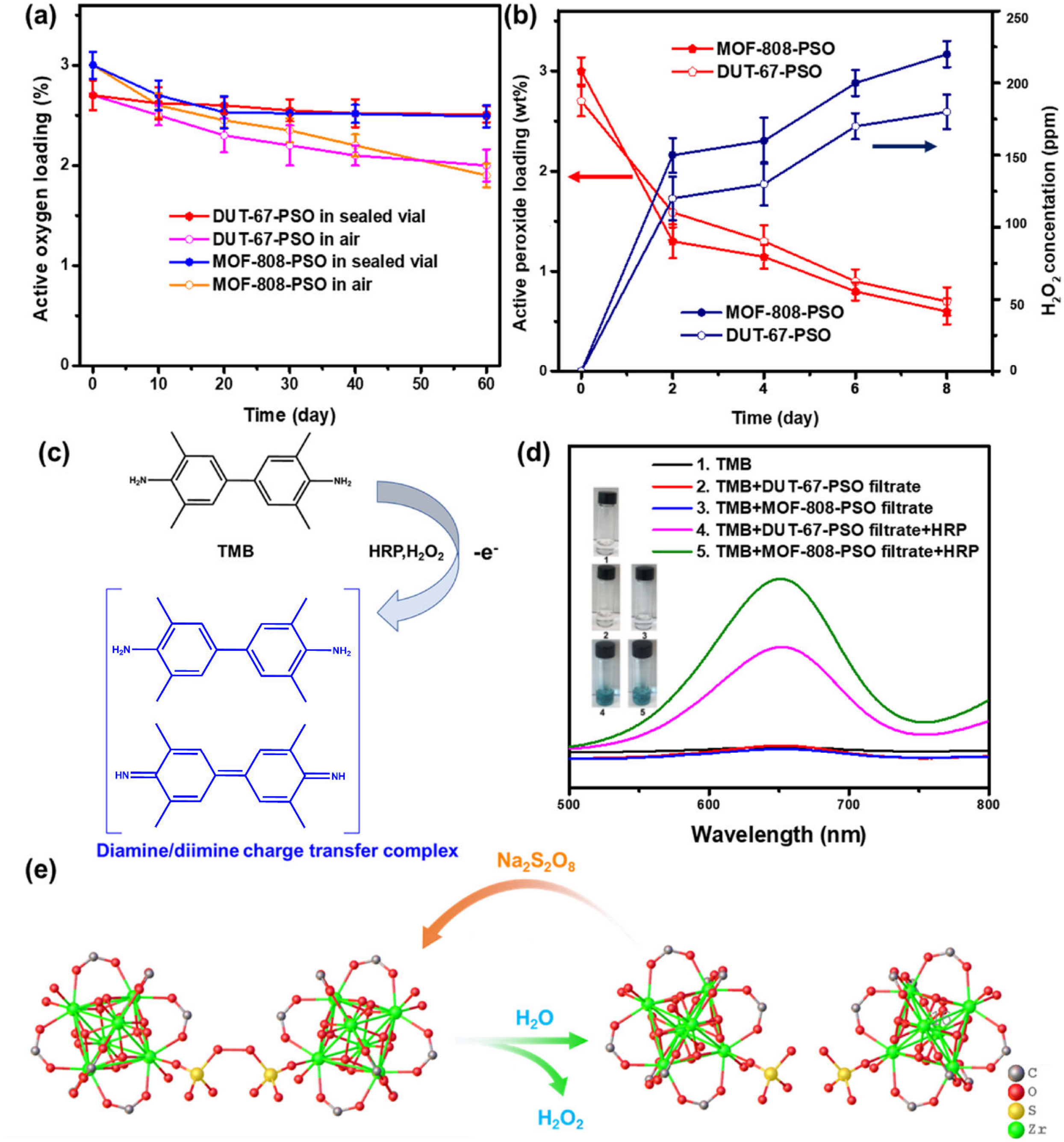

Figure 3. (a) Storage stability of active peroxide-loaded MOF-PSO powders in a sealed vial and in air. (b) Storage stability of active peroxide-loaded MOF-PSO powders in 0.90 wt% saline water. (c) Horseradish peroxidase (HRP)-catalyzed tetramethylbenzidine (TMB) oxidation reaction used to identify released active species. (d) UV-vis absorption spectra and photograph

images of the TMB solutions oxidized by different filtrates with or without HRP enzyme after 5 min reaction. (e) Proposed biocidal hydrogen peroxide release and PSO regeneration mechanism.

Stability of Hydrogen Peroxide in the MOF Carriers

The stability of active peroxide precursor in the MOF carrier is critical for practical application as it dictates the shelf life of the products.[23-25] Quantification titration tests indicate that DUT-67-PSO and MOF-808-PSO retained above 90% of the initial active peroxide loading after storage in a sealed vial in a desiccator for 40 days, which indicates that these PSO-loaded Zr-MOFs are very stable under proper storage conditions (Figure 3a). To achieve biocidal activity in practical and real-world conditions, the biocidal peroxide species needs to be released upon exposure to humidity. Therefore, we also tested the active peroxide precursor concentration after DUT-67-PSO and MOF-808-PSO were exposed to 65% relative humidity (RH) for 40 days and found that they kept 60% and 75% active peroxide loading, respectively, indicating good stability of the PSO under humid air (Figure 3a and Figure S8). The accelerated release test in 0.9 wt% saline water showed a half-life of about two days of the active peroxide content in these two PSO loaded Zr-MOFs (Figure 3b). To demonstrate that the release of the active species is hydrogen peroxide, we conducted a chromogenic catalysis of tetramethylbenzidine (TMB), which could be selectively oxidized into a blue complex of TMB and diimine by hydrogen peroxide in presence of horseradish peroxidase (HRP) as the catalyst (Figure 3c).[48-49] When a TMB solution (in 0.1 M acetate buffer, pH 3.6) was mixed with filtrates from DUT-67-PSO and MOF-808-PSO, no obvious color changes were observed. However, after the addition of peroxidase, the color turned blue, with a characteristic absorption wavelength at 652 nm for the TMB diimine complex, indicating the presence of hydrogen peroxide as the oxidant in the catalytic reaction (Figure 3d). Interestingly, a bright yellow color was observed when the TMB solution was mixed with sodium persulfate dissolved in 0.9 wt% saline water (with the equivalent peroxide in the MOF-808-PSO filtrate), which could further rule out the presence of persulfate in the filtrates from the MOF-PSO system (Figure S7). Moreover, ICP-OES analysis indicates that the relative atomic ratio of S to Zr on MOF-PSO remains unchanged after the treatment with saline water, suggesting that these MOFs release hydrogen peroxide upon *in situ* hydrolysis of the coordinated persulfates, rather than through the direct release of PSO from MOF nodes, which is consistent with the production of hydrogen peroxide with persulfates as the intermediates (Figure 3e and Figure

S8).[50] Importantly, the active peroxide lost during storage and saline water treatment could be fully recharged by another sodium persulfate solution treatment, which means this MOF-PSO system is regeneratable (Figure 3e). We also tested the ability of the PSO to be regenerated for multiple cycles in the Zr-MOF carrier following discharge of the peroxide species. To probe this, we quenched the active peroxide precursor through the addition of an excess aqueous sodium thiosulfate solution to PSO-loaded Zr-MOF, and we confirmed there was no active PSO remaining in the MOF after quenching using a KI test. The quenched Zr-MOF was then regenerated with an aqueous sodium persulfate solution (Figure S9). For both Zr-MOF carriers, the active peroxide loadings for freshly prepared samples were similar to those of samples subjected to five quench-regeneration cycles, indicating good renewability of the active peroxide precursors in these frameworks (Figure S9). Moreover, the PXRD patterns obtained following the 5th quench-regeneration cycle are similar to the simulated patterns, indicating no loss in crystallinity after repeated regeneration cycles (Figure S10).

MOF/fiber composite synthesis and antibacterial activity

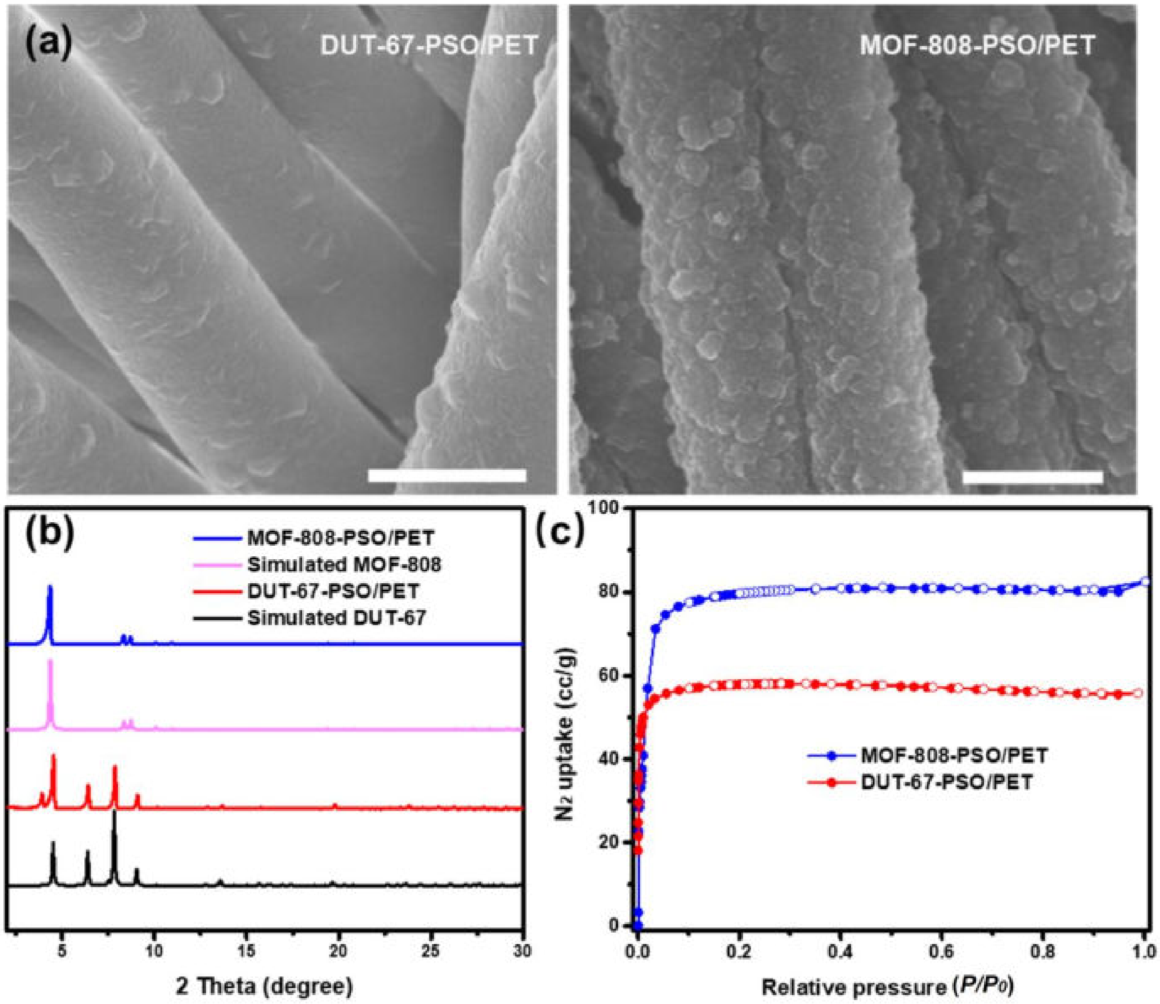

Figure 4. (a) SEM images, (b) PXRD patterns and (c) N_2 sorption isotherms of DUT-67-PSO/PET and MOF-808-PSO/PET. Scale bars: 15 µm.

The successful immobilization of regenerable active peroxide precursors into Zr-MOF carriers encouraged us to integrate these Zr-MOFs onto textiles to probe the utility of this approach for biocidal textiles that operate under practical conditions.[51-59] To begin, we coated a commercial polyethylene terephthalate (PET) cloth with DUT-67 and MOF-808, denoted as DUT-67/PET and MOF-808/PET, respectively, by using an eco-friendly aqueous growth method (Figure S11).[25,56] Briefly, we mixed polyester fabrics with the organic linker, zirconium salt, and an organic acid as a modulator in DI water, then heated the mixture in an oven at 100 °C for 6 h. Continuous intergrown polycrystalline coatings with thicknesses of about 2 µm formed on the fiber surfaces, as observed through SEM imaging (Figure S12-S15). PXRD studies verified the crystalline nature of the desired MOF phase (Figure S11 and FigureS13), and ICP-OES studies indicated MOF mass loadings of 25 wt% and 26 wt% for DUT-67/PET and MOF-808/PET, respectively. In addition, N_2 sorption isotherms confirmed that the MOFs remain porous in these composites (Figure S12 and Figure S15).

After confirming the successful integration of Zr-MOFs onto the PET fabric, we then loaded PSO into the composites using an analogous procedure employed for powdered Zr-MOF samples. This sodium persulfate solution treatment afforded a 0.50 wt% and 0.72 wt% loading of the active peroxide into the MOF/PET composites, which we denoted as DUT-67-PSO/PET and MOF-808-PSO/PET. SEM images of these composites reveal no obvious changes to the morphology (Figure S12 and Figure S14 and Figure 4a), which is consistent with the results from the powdered PSO-loaded MOF samples. Similarly, PXRD analysis and N_2 sorption isotherms confirm the crystalline and porous nature, respectively, of the DUT-67-PSO/PET and MOF-808-PSO/PET composites (Figure 4b-c). Notably, the composite textile materials retained their original white color after PSO loading (Figure S11) and do not emit an unpleasant odor, highlighting the potential usefulness of this strategy in practical settings.

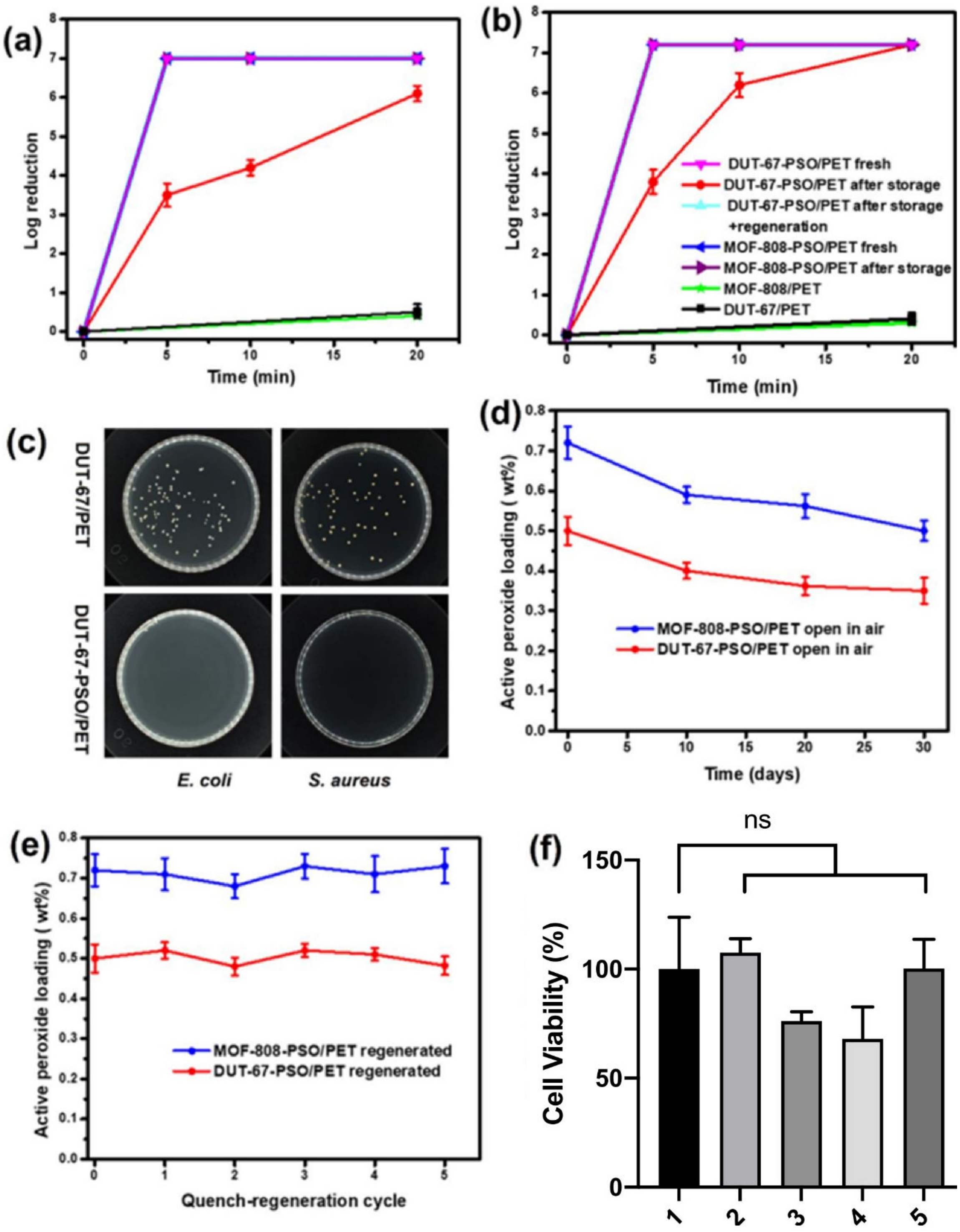

Figure 5. Antibacterial activities of control samples and Zr-MOF-PSO/PET composites against (a) *E. coli* and (b) *S. aureus*. Storage conditions: 65% RH for 30 days. (c) Representative agar plates with the colonies from control and PSO loaded sample. (d) Storage stability and (e) regenerability of active peroxide in the DUT-67-PSO/PET and MOF-808-PSO/PET composite. (f) Cell viability of HEKn cells

following 24 h treatment with samples: 1 uncoated PET, 2 DUT-67/PET, 3 MOF-808/PET, 4 DUT-67-PSO/PET and 5 MOF-808-PSO/PET. All treatments normalized to uncoated PET. ns = not significant.

Antibacterial Activity

With the PSO-loaded composites in hand, we then evaluated their antimicrobial performance against Gram-negative *Escherichia coli* (*E. coli*) and Gram-positive *Staphylococcus aureus* (*S. aureus*) bacteria using a modified American Association of Textile Chemists and Colorists (AATCC) test protocol AATCC-100–2004.[23-25] The composite samples (1 cm × 1 cm) were challenged with 10 μL of a bacterial suspension (~10^7 colony-forming units (CFU)/mL) for 5 min to 20 min, after which the bacteria were extracted from the fiber composites. The antibacterial activity was determined based on the viable microbial colony counting method and summarized in Figure 5a, b.[23-25] The control sample, PSO-free DUT-67/PET and MOF-808/PET, exhibit no obvious biocidal effects (Figure 5a,b). In contrast, the freshly prepared DUT-67-PSO/PET and MOF-808-PSO/PET composites show fast and potent antimicrobial activities against both Gram-negative and Gram-positive bacteria, demonstrating a 7-log (100%) reduction against *E. coli* and *S. aureus* after only 5 min contact (Figure 5a, b). In sharp contrast to the control samples, representative agar plates demonstrate the total killing of the two bacteria strains by the PSO-loaded Zr-MOF coatings (Figure 5c and Figure S16). Moreover, we observed morphological changes by SEM in the bacteria after treatment with PSO-loaded samples. Specifically, *S. aureus* and *E. coli* retained spherical and corynebacterium morphologies, respectively, after exposure to the control samples, while the bacteria treated with the PSO-loaded coatings show obvious cellular deformation and membrane collapse (Figure S17).

Since the loss of active peroxide precursors in the protective cloths during storage could degrade biocidal efficacy, we investigated the stability of active peroxide precursors in the DUT-67-PSO/PET and MOF-808-PSO/PET cloths. To further demonstrate the practicality of this composite material in real-world applications, we exposed the composite to air at 65% RH for 30 days and found that about 70% of the original active peroxide content remains in both samples (Figure 5d). After 30 days of storage, MOF-808-PSO/PET maintains 0.52 wt% active peroxide, which is similar to the active peroxide loading of fresh DUT-67-PSO/PET before storage (0.5 wt%). Notably, after storing MOF-808-PSO/PET for 30 days, this composite achieved total killing of both strains after 5 min, indicating the same biocidal activity as the fresh sample. We found that after storing DUT-67-PSO/PET for 30 days in humid air, this composite retained 0.35 wt% active peroxide loading compared to 0.5 wt% for the fresh sample. This decrease in loading results in slightly reduced antimicrobial potency for this composite against Gram-positive and Gram-negative strains relative to that of the fresh sample. After 10 min contact, the aged DUT-67-PSO/PET sample achieved a ~4-log (99.99%) reduction of *E. coli* and a ~6-log (99.9999%) reduction of *S. aureus* (Figure 5a-b). Gram-negative bacteria possess a protective cell wall with an outer lipopolysaccharide membrane, which could reduce the antimicrobial agent penetration into the cell and show more resistance to oxidative biocides.[60-61]

Due to its relatively higher initial peroxide loading, MOF-808-PSO/PET can fully maintain its antibacterial performance after storage. Importantly, after re-treating aged DUT-67-PSO/PET with a sodium persulfate solution, the active peroxide precursor loading lost during storage was recovered, and the antibacterial activity was fully restored (Figure 5a-b). To further evaluate the renewability of active peroxide species in the two Zr-MOF-coated PET fabrics, we quenched the active peroxide precursors of fresh PSO-loaded samples using an aqueous sodium thiosulfate water solution and then regenerated the active peroxide precursors upon treatment with an aqueous sodium persulfate solution. After five quenching and regeneration cycles, the same active peroxide loading could be fully recovered (Figure 5e). Moreover, PXRD analysis, SEM imaging, and ICP-OES results confirm that the crystallinity, surface morphology, and mass loading, respectively, of the two Zr-MOFs coatings in these PET composites remains unchanged after five regeneration cycles, demonstrating the excellent renewability and durability of the PSO-loaded Zr-MOF/PET composite (Figure S18-S21). Importantly, we didn't observe any dusting or detachment of the MOF coating during first PSO loading and regeneration sequence, which can likely be attributed to the improved stability that results from the morphology of the intergrown MOF coating on the PET fibers. To evaluate the biocompatibility of these Zr-MOF- and Zr-MOF-PSO-coated fibers, we next assessed their cytotoxicity with HEKn cells as a model mammalian cell line (Figure 5f).[62] Following overnight incubation of cells on fibers, we did not observe any significant differences in cell viability between the different groups (uncoated PET, DUT-67/PET, MOF-808/PET, DUT-67-PSO/PET and MOF-808-PSO/PET). Combined, these results indicate that the Zr-MOF coatings, both with and without PSO, do not noticeably impact cell performance, thereby demonstrating biocompatibility of this composite system with mammalian cells. In practical applications, a layer of barrier textile could be used to avoid direct contact between skin and active antibacterial textile layer. At the same time, these antibacterial textiles could be used in wider application fields without direct contact with human skin, such as in filters for air purification and internal cloths (e.g., curtains).

Conclusion

We introduced a versatile strategy to access nanoporous Zr-MOFs loaded with persulfate ion carriers that act as active peroxide precursors and release biocidal hydrogen peroxide upon exposure to humidity, endowing these Zr-MOFs with antibacterial properties. Single crystal X-ray diffraction studies revealed a distinct PSO coordination geometry for each Zr-MOF (e.g., one PSO bridges across two adjacent nodes in DUT-67, while one PSO coordinates in a bidentate fashion to a single node in MOF-808) that is dependent on node connectivity and distances between possible coordination sites. Despite these differences, both Zr-MOFs exhibit comparable PSO loadings that can be regenerated for at least five cycles with no apparent loss in PSO capacity. We leveraged these properties to develop biocidal textile composites by integrating MOF coatings onto commercial textile fibers and treating them with an aqueous sodium persulfate solution. These PSO-loaded MOF/fiber composites demonstrate excellent, broad-spectrum biocidal performance against Gram-positive and Gram-negative bacteria and good biocompatibility. Importantly, storage of these composites for several weeks under ambient conditions does not significantly diminish the PSO loading or the biocidal activity of the composite. Moving forward, this strategy to develop regenerable biocidal composite textiles may potentially provide highly effective protective gear for use in high-risk settings, such as in hospitals or elderly care homes, while reducing the solid waste generated from traditional, single-use protective masks and cloths currently used around the world today.

Experimental Section

General Procedure for Preparation of DUT-67-PSO and MOF-808-PSO

5% sodium persulfate solution was used to load the persulfate ion, namely the active hydrogen peroxide precursor, onto Zr-MOF powders. 0.2 g Zr-MOF (DUT-67 or MOF-808) was immersed in 500 mL sodium persulfate water solution at room temperature for 24 h. The powder was washed using DI water three times to remove unreacted species, and then washed using acetone three times and dried in a hood overnight to obtained DUT-67-PSO and MOF-808-PSO, respectively. All samples were and stored under vacuum at room temperature before use.

Synthesis of DUT-67-PSO/PET

Four pieces of PET textile (4 cm x 4 cm), 2,5-thiophenedicarboxylic acid (26.6 mmol, 4.6 g), and $ZrOCl_2 \cdot 8H_2O$ (40 mmol, 12.9 g) were mixed in DI water (100 mL) and acetic acid (AA) (100 mL) and then sealed in a 500 mL Pyrex Schott bottle. After sonication for 0.5 h, the mixture was placed in an oven at 100 °C for 6 h. After cooling down, the composite samples were washed by deionized water (2 x 50 mL) and acetone (3 x 50 mL). Finally, the composite samples were dried at room temperature and stored under vacuum at room temperature. One piece of Zr-MOF coated fiber composite (5 cm x 5 cm) was immersed in 500 mL of 5% sodium persulfate water solution at room temperature for 24 h and washed using DI water three times to remove unreacted species, and then washed using acetone three times and dried in a hood overnight. All samples were and stored under vacuum at room temperature before use.

Synthesis of MOF-808-PSO/PET

Trimesic acid (4 mmol, 0.84 g) was added to a mixture of DI water (40 mL) and TFA (30 mL) in a sealed 200 mL flask and refluxed for 1 hour to totally dissolve the solid. The solution was transferred to a 250 mL Pyrex Schott bottle. $ZrOCl_2 \cdot 8H_2O$ (9 mmol, 2.9 g) and four pieces of PET textile (4 cm x 4 cm) were added to above mixture. The sealed bottle was placed place in an oven at 100 °C for 6 h. After cooling down to room temperature, the obtained fabric samples washed by deionized water (2 x 100 mL), acetone (3 x 100 mL). Finally, the samples were dried at room temperature. One piece of Zr-MOF coated fiber composite (5 cm x 5 cm) was immersed in 500 mL of 5% sodium persulfate water solution at room temperature for 24 h and washed using DI water three times to remove unreacted species, and then washed using acetone three times and dried in a hood overnight. All samples were and stored under vacuum at room temperature before use.

Supporting Information

Additional materials synthesis, antibacterial method, and characterization data, including PXRD, SEM, sample photographs etc. are available in Supporting Information.

Corresponding Authors

Kaikai Ma, Email: kaikai.ma@northwestern.edu
Yuk Ha Cheung, Email: yh-yuki.cheung@polyu..edu.hk

John H. Xin, Email: tcxinjh@polyu.edu.hk
Omar K. Farha, Email: o-farha@northwestern.edu

Author Contributions

[#]K.M, Y.H.C and H.X contributed equally to this work.

Notes

The authors declare the following competing financial interest(s): O.K.F. has a financial interest in the start-up company Nu-Mat Technologies, which is seeking to commercialize metal-organic frameworks.

ACKNOWLEDGMENTS

The authors acknowledge the financial support from the Army Research Office (W911NF1910340) and the Northwestern University Institute for Catalysis in Energy Processes (ICEP), funded by the DOE, Office of Basic Energy Sciences (Award Number DE-FG02- 03ER15457). This work made use of the J.B. Cohen X-ray Diffraction Facility supported by the MRSEC program of the National Science Foundation (DMR-1720139) at the Materials Re-search Center of Northwestern University. This work made use of Keck-II and EPIC facilities of the NUANCE Center at Northwestern University, which has received support from the Soft and Hybrid Nanotechnology Experimental (SHyNE) Resource (NSF NNCI-1542205); the MRSEC pro-gram (NSF DMR-1720139) at the Materials Research Center; the International Institute for Nanotechnology (IIN); the Keck Foundation; and the State of Illinois, through the IIN. This work made use of the IMSERC at Northwestern University, which has received support from the NSF (CHE-1048773 and DMR-0521267); the State of Illinois and IIN. K.O.K. gratefully acknowledges support from the IIN Postdoctoral Fellowship and the Northwestern University International Institute for Nanotechnology. J.H.X. acknowledges the support from General Research Fund of the Research Grants Council of the Hong Kong SAR Government (GRF 15208420). M.E. was partially supported by the Alexander S. Onassis Public Benefit Foundation. The authors acknowledge Dr. Timur Islamoglu for the helpful discussion.

Reference

[1] P. S. Loomba, J. Taneja, B. Mishra, Methicillin and Vancomycin Resistant S. aureus in Hospitalized Patients *J. Glob. Infect. Dis.* **2010,** *2*, 275-283.

[2] A. B. Edward, T. O. Michael, COVID-19 and Flu, A Perfect Storm. *Science* 2020, *368*, 1163-1163.

[3] R. J. Melander, C. Melander, The Challenge of Overcoming Antibiotic Resistance: An Adjuvant Approach? *ACS Infect. Dis.* **2017,** *3*, 559-563.

[4] C. J. E. Metcalf, J. Lessler, Opportunities and Challenges in Modeling Emerging Infectious Diseases. *Science* **2017,** *357*, 149-152.

[5] D. Mallick, D. Gupta, S Sharma, Transfer of Bacteria Between Fabric and Surrogate Skin. *Am. J. Infect. Control.* **2022,** *50***,** 758-763.

[6] G. Kampf, World Health Organization Declares Global Emergency: A Review of the 2019 Novel Coronavirus (COVID-19). *GMS Hyg. Infect. Control* **2020**, *15*, Doc10.

[7] A. Hanczvikkel, A. Víg, A. Tóth, Survival Capability of Healthcare-Associated, Multidrug-Resistant Bacteria on Untreated and on Antimicrobial Textiles. *J. Ind. Text.* 2019, **48**, 1113.

[8] O. Koca, U. Altoparlak, A. Ayyildiz, H. Kaynar, Persistence of Nosocomial Pathogens on Various Fabrics. *Eurasian J. Med.* **2012,** *44*, 28-31.

[9] Gulati R, Sharma S, Sharma RK. Antimicrobial Textile: Recent Developments and Functional Perspective. *Polym Bull*. 2021; **2021**: 1-25

[10] M. Liang, F. Wang, M. Liu, J. Yu, Y. Si, B. Ding, N-Halamine Functionalized Electrospun Poly(Vinyl Alcohol-co-Ethylene) Nanofibrous Membranes with Rechargeable Antibacterial Activity for Bioprotective Applications. *Adv. Fiber Mater.* **2019**, *1*, 126.

[11] S. G. Wang, F. Y. Zheng, Y. P. Huang, Y. T. Fang, M. W. Shen, M. F. Zhu, X. Y. Shi, Encapsulation of Amoxicillin within Laponite-Doped Poly(lactic-co-glycolic acid) Nanofibers: Preparation, Characterization, and Antibacterial Activity. *ACS Appl. Mater. Interfaces* **2012**, *4*, 11, 6393–6401

[12] X. Wang, K. Ma, T. Goh, M. R. Mian, H. Xie, H. Mao, J. Duan, K. O. Kirlikovali, A. E. B. S. Stone, D.Ray, M. R. Wasielewski, L. Gagliardi, O.K. Farha, Photocatalytic Biocidal Coatings Featuring Zr_6Ti_4-Based Metal–Organic Frameworks. *J. Am. Chem. Soc.* **2022**, 144, 12192–12201.

[13] N. Karim, S. Afroj, K. Lloyd, L. C. Oaten, D. V. Andreeva, C. Carr, A. D. Farmery, I.D. Kim, K.S. Novoselov, Sustainable Personal Protective Clothing for Healthcare Applications: A Review. *ACS Nano* **2020**, *14*, 12313−12340.

[14] C. R. Jabbour, L. A. Parker, E. M. Hutter, B. Weckhuysen, Chemical Targets to Deactivate Biological and Chemical Toxins Using Surfaces and Fabrics. *Nat. Rev. Chem*. **2021**, *5*, 370–387.

[15] G. Peterson, D. T. Lee, H. F. Barton, T. H. Epps, G. Parsons, Fibre-based Composites from The Integration of Metal–Organic Frameworks and Polymers. *Nat. Rev. Mater.* **2021**, 6, 605-621.

[16] B. Balasubramaniam, S. Prateek, Ranjan, M. Saraf, P. Kar, S. P. Singh, V. K. Thakur, A. Singh, R. K. Gupta, Antibacterial and Antiviral Functional Materials: Chemistry and Biological Activity Toward Tackling covid-19-like Pandemics. *ACS Pharmacol. Transl. Sci.* **2021**, *4*, 8-54.

[17] L. Huang, S. Xu, Z. Wang, K. Xue, J. Su, Y. Song, S. Chen, C. Zhu, B. Z. Tang, R. Ye, Self-Reporting and Photothermally Enhanced Rapid Bacterial Killing on A Laser-induced Graphene Mask. *ACS Nano* **2020,** *14*, 12045-12053.

[18] P. Tang, Z. Zhang, A. Y. El-Moghazy, N. Wisuthiphaet, N. Nitin, G. Sun, Daylight-induced Antibacterial and Antiviral Cotton Cloth for Offensive Personal Protection. *ACS Appl. Mater. Interfaces* **2020,** *12*, 49442-49451.

[19] Y. Wang, K. Ma, J. Bai, T. Xu, W. Han, C. Wang, Z. Chen, K. O. Kirlikovali, P. Li, J. Xiao, O. K. Farha, Chemically Engineered Porous Molecular Coatings as Reactive Peroxide Species Generators and Reservoirs for Long-Lasting Self-Cleaning Textiles. *Angew. Chem., Int. Ed.* **2022**, *61*, No. e202115956.

[20] Y. Si, Z. Zhang, W. Wu, Q. Fu, K. Huang, N. Nitin, B. Ding, G. Sun, Daylight-driven Rechargeable Antibacterial and Antiviral Nanofibrous Membranes for Bioprotective Applications. *Sci. Adv.* **2018,** *4*, eaar5931.

[21] Z. B. Cao, X. B. Sun, J. R. Yao, Y. Y. Sun, Silver Sulfadiazine Immobilized Celluloses as Biocompatible Polymeric Biocides. *J. Bioact. Compat. Polym.* **2013**, *28*, 398−409.

[22] Z. Chen, J. Luo, Y. Sun, Biocidal Efficacy, Biofilm-Controlling Function, And Controlled Release Effect of Chloromelamine-Based Bioresponsive Fibrous Materials. *Biomaterials* **2007**, *28*, 1597−1609.

[23] L. Huang, G. Sun, Durable and Oxygen Bleach Rechargeable Antimicrobial Cellulose: Sodium Perborate as An Activating and Recharging Agent. *Ind. Eng. Chem. Res.* **2003**, *42*, 5417-5422.

[24] Q. Borjihan, J. Yang, Q. Song, L. Gao, M. Xu, T. Gao, W. Liu, P. Li, Q. Li, A. Dong, Povidone-Iodine-Functionalized Fluorinated Copolymers with Dual-Functional Antibacterial and Antifouling Activities. *Biomater. Sci.* **2019**, *7*, 3334-3347.

[25] Y. H. Cheung, K. Ma, H. C. van Leeuwen, M. C. Wasson, X. Wang, K. B. Idrees, W. Gong, R. Cao, J. J. Mahle, T. Islamoglu, G. W. Peterson, M. C. de Koning, J. H. Xin, O. K. Farha. Immobilized Regenerable Active Chlorine within a Zirconium-Based MOF Textile Composite to Eliminate Biological and Chemical Threats. *J. Am. Chem. Soc.* **2021,** *143*, 16777-16785.

[26] H. Furukawa, K. E. Cordova, M. O'Keeffe, O. M. Yaghi, The Chemistry and Applications of Metal-Organic Frameworks. *Science* **2013**, *341*, 1230444.

[27] M. Eddaoudi, J. Kim, N. Rosi, D. Vodak, J. Wachter, M. O'Keeffe, O. M. Yaghi, Systematic Design of Pore Size and Functionality in Isoreticular MOFs and their Application in Methane Storage. *Science* **2002,** *295*, 469-472.

[28] C. Serre, F. Millange, C. Thouvenot, M. Noguès, G. Marsolier, D. Louër, G. Férey, Very Large Breathing Effect in the First Nanoporous Chromium(III)-Based Solids: MIL-53 or $Cr^{III}(OH)\cdot\{O_2C{-}C_6H_4{-}CO_2\}\cdot\{HO_2C{-}C_6H_4{-}CO_2H\}_x\cdot H_2O_y$ *J. Am. Chem. Soc.* **2002**, *124,* 13519-13526.

[29] G. Distefano, H. Suzuki, M. Tsujimoto, S. Isoda, S. Bracco, A. Comotti, P. Sozzani, T. Uemura, S. Kitagawa, Highly Ordered Alignment of a Vinyl Polymer by Host-Guest Cross-Polymerization. *Nat. Chem.* **2013**, *5*, 335-341.

[30] D. Alezi, Y. Belmabkhout, M. Suyetin, P. M. Bhatt, L. J. Weselinski, V. Solovyeva, K. Adil, I. Spanopoulos, P. N. Trikalitis, A. H. Emwas, M. Eddaoudi, MOF Crystal Chemistry Paving the Way to Gas Storage Needs: Aluminum-Based soc-MOF for CH_4, O_2, and CO_2 Storage. *J. Am. Chem. Soc.* **2015**, *137*, 13308-13318.

[31] T. Islamoglu, Z. Chen, M. C. Wasson, C. T. Buru, K. O. Kirlikovali, U. Afrin, M. R. Mian, O. K. Farha, Metal–Organic Frameworks against Toxic Chemicals. *Chem. Rev.* **2020**, *120*, 8130-8160.

[32] X. Lian, Y. Fang, E. Joseph, Q. Wang, J. Li, S. Banerjee, C. Lollar, X. Wang, H.-C. Zhou, Enzyme–MOF (Metal–Organic Framework) Composites. *Chem. Soc. Rev.* **2017**, *46*, 3386.

[33] X. Wang, P. C. Lan, S. Ma, Metal–Organic Frameworks for Enzyme Immobilization. *ACS Cent. Sci.* **2020**, *6*, 1497–1506.

[34] M. H. Teplensky, M. Fantham, P. Li, T. C. Wang, J. P. Mehta, L. J. Young, P. Z. Moghadam, J. T. Hupp, O. K. Farha, C. F. Kaminski, D. Fairen-Jimenez. Temperature Treatment of Highly Porous Zirconium-Containing Metal–Organic Frameworks Extends Drug Delivery Release. *J. Am. Chem. Soc.* **2017**, *139*, 7522−7532.

[35] Y. Chen, P. Li, J. A. Modica, R. J. Drout, O. K. Farha. Acid-Resistant Mesoporous Metal–Organic Framework toward Oral Insulin Delivery: Protein Encapsulation, Protection, and Release. *J. Am. Chem. Soc.* **2018**, *140*, 5678−5681.

[36] A. C. McKinlay, B. Xiao, D. S. Wragg, P. S. Wheatley, I. L. Megson, R. E. Morris. Exceptional Behavior over the Whole Adsorption−Storage−Delivery Cycle for NO in Porous Metal Organic Frameworks. *J. Am. Chem. Soc.* **2008**, *130*, 10440-10444.

[37] B. Zhang, H.W. Chen, Q.H. Hu, L.M. Jiang, Y.Q. Shen, D. Zhao, Z. X. Zhou. CelluMOFs: Green, Facile, and Flexible Metal-Organic Frameworks for Versatile Applications. *Adv. Funct. Mater.*, **2021**, *31*, 2105395.

[38] M. Nakhaei, K. Akhbari, A. Davoodi. Biocompatible MOF-808 as An Iodophor Antimicrobial Agent with Controlled and Sustained Release of Iodine. *CrystEngComm* **2021**, *23*, 8538−8545.

[39] A.N. Au-Duong, C.K. Lee, Iodine-loaded Metal Organic Framework as Growth-triggered antimicrobial Agent. *Mater. Sci. Eng. C* **2017**, *76*, 477–482.

[40] J. Jiang, F. Gándara, Y.B. Zhang, K. Na, O. M. Yaghi, W. G. Klemperer, Superacidity in Sulfated Metal–Organic Framework-808. *J. Am. Chem. Soc.* **2014**, *136*, 12844−12847.

[41] V. Bon, I. Senkovska, I. A. Baburin, S. Kaskel. Zr- and Hf-Based Metal–Organic Frameworks: Tracking Down the Polymorphism. *Cryst. Growth Des.* **2013**, *13*, 1231– 1237.

[42] K. Otake, J. Ye, M. Mandal, T. Islamoglu, C. T. Buru, J. T. Hupp, M. Delferro, D. G. Truhlar, C. J. Cramer, O. K. Farha. Enhanced Activity of Heterogeneous Pd(II) Catalysts on Acid-Functionalized Metal–Organic Frameworks. *ACS Catal.* **2019**, *9*, 5383−5390.

[43] CCDC-2176214 (DUT-67-PSO) and CCDC-2176215 (MOF-808(Hf)-PSO) with the supplementary crystallographic data for this paper can be obtained free of charge from The Cambridge Crystallographic Data Centre.

[44] A. Singh, R. P. Sharma, V. Ferretti, S. Rossetti, P. Venugopalan. Anion binding through second sphere coordination: Synthesis, Characterization and X-ray Structures of Cationic Carbonato Bis(1,10-phenanthroline)cobalt(III) Complex with Sulphur Oxoanions. *J. Mol. Struct.* **2009**, *927*, 111-120.

[45] J. L. Manson, K. H. Stone, H. I. Southerland, T. Lancaster, A. J. Steele, S. J. Blundell, F. L. Pratt, P. J. Baker, R. D. McDonald, P. Sengupta, J. Singleton, P. A. Goddard, C. Lee, M.H. Whangbo, M. M. Warter, C. H. Mielke, P. W. Stephens. Characterization of the Antiferromagnetism in Ag(pyz)2(S2O8) (pyz = Pyrazine) with a Two-Dimensional Square Lattice of Ag^{2+} Ions. *J. Am. Chem. Soc.* **2009,** *131*, 4590-4591.

[46] J. P. Carpenter, C. T. McTernan, T. K. Ronson, J. R. Nitschke, Anion Pairs Template a Trigonal Prism with Disilver Vertices. *J. Am. Chem. Soc.* **2019,** *141*, 11409-11413.

[47] E. Torti, V. Havel, M. A. Yawer, L. Ludvíková, M. Babiak, P. Klán, V. Sindelar, Supramolecular Storage and Controlled Photorelease of an Oxidizing Agent using a Bambusuril Macrocycle. *Chem. Eur. J.* **2017,** *23*, 16768-16772.

[48] F. Olucha, F. Martínez-García, C. López-García, A New stabilizing agent for the tetramethyl Benzidine (TMB) Reaction Product in the Histochemical Detection of Horseradish Peroxidase (HRP). *J. Neurosci. Methods* **1985**, **13,** 131–138.

[49] L. Gao, J. Zhuang, L. Nie, J. Zhang, Y. Zhang, N. Gu, T. Wang, J. Feng, D. Yang, S. Perrett, X. Yan. Intrinsic Peroxidase-Like Activity of Ferromagnetic Nanoparticles. *Nat. Nanotechnol.* **2007**, 2, 577– 583.

[50] Jones, C. W. *Applications of Hydrogen Peroxide and Derivatives* (eds Clark, J. H. & Braithwaite, M. J.) 1–34 (Royal Society of Chemistry, **1999**).

[51] Z. Chen, K. Ma, J. J. Mahle, H. Wang, Z. H. Syed, A. Atilgan, Y. Chen, J. H. Xin, T. Islamoglu, G. W. Peterson, O. K. Farha. Integration of Metal–Organic Frameworks on Protective Layers for Destruction of Nerve Agents under Relevant Conditions. *J. Am. Chem. Soc.* **2019**, *141*, 20016-20021.

[52] Y. Chen, S. Zhang, S. Cao, S. Li, F. Chen, S. Yuan, C. Xu, J. Zhou, X. Feng, X. Ma, B. Wang. Roll-to-Roll Production of Metal-Organic Framework Coatings for Particulate Matter Removal. *Adv. Mater.* **2017**, *29*, 1606221.

[53] P. Li, J. Li, X. Feng, J. Li, Y. Hao, J. Zhang, H. Wang, A. Yin, J. Zhou, X. Ma, B. Wang. Metal-Organic Frameworks with Photocatalytic Bactericidal Activity for Integrated Air Cleaning. *Nat. Commun.* **2019**, *10*, 2177.

[54] X. Ma, Y. Chai, P. Li, B. Wang. Metal–Organic Framework Films and Their Potential Applications in Environmental Pollution Control. *Acc. Chem. Res.* **2019**, *52*, 1461−1470.

[55] H. Wang, P. Rassu, X. Wang, H. Li, X. Wang, X. Wang, X. Feng, A. Yin, P. Li, X. Jin, S. L. Chen, X. Ma, B. Wang. An Iron-Containing Metal-Organic Framework as a Highly Efficient Catalyst for Ozone Decomposition. *Angew. Chem., Int. Ed.* **2018**, *57*, 16416-16420.

[56] K. Ma, T. Islamoglu, Z. Chen, P. Li, M. C. Wasson, Y. Chen, Y. Wang, G. W. Peterson, J. H. Xin, O. K. Farha. Scalable and Template-Free Aqueous Synthesis of Zirconium-Based Metal-Organic Framework Coating on Textile Fiber. *J. Am. Chem. Soc.* **2019**, *141*, 15626-15633.

[57] K. Ma, M. C. Wasson, X. Wang, X. Zhang, K. B. Idrees, Z. Chen, Y. Wu, S. Lee, R. Cao, Y. Chen, L. Yang, F. A. Son, T. Islamoglu, G. W. Peterson, J. J. Mahle, O. K. Farha. Near-instantaneous catalytic hydrolysis of organophosphorus nerve agents with zirconium-based MOF/hydrogel composites. *Chem Catalysis.* **2021**, *1,* 721-733.

[58] D.T. Lee, J. D. Jamir, G. W. Peterson, G. N. Parsons, Protective Fabrics: Metal-Organic Framework Textiles for Rapid Photocatalytic Sulfur Mustard Simulant Detoxification. *Matter* **2020**, *2*, 404−415.

[59] Y. Zhang, S. Yuan, X. Feng, H. Li, J. Zhou, B. Wang. Preparation of Nanofibrous Metal–Organic Framework Filters for Efficient Air Pollution Control. *J. Am. Chem. Soc.* **2016**, *138*, 5785-5788.

[60] S. Denyer, G. Stewart, Mechanisms of Action of Disinfectants. *Int. Biodeterior. Biodegrad.* **1998**, *41*, 261-268.

[61] S. Denyer, Mechanisms of Action of Antibacterial Biocides. *Int. Biodeterior. Biodegrad.* **1995**, *36*, 227-245.

[62] I.K. Maurya, S. Singh, R. Tewari, M. Tripathi, S. Upadhyay, Y. Joshi. Antimicrobial activity of Bulbothrix setschwanensis (Zahlbr.) Hale lichen by cell wall disruption of Staphylococcus aureus and Cryptococcus neoformans. *Microb. Pathog.* **2018**, *115*, 12-18.

TOC